Open Access

Recent Progress in Materials

LIDSEN Publishing Inc.

Review

Wave Propagation and Scattering due to Debonding in CFRP Strengthened Reinforced Concrete Beams

Evelyne El Masri [1,*], Tat-Hean Gan [2]

1. Brunel University London, Uxbridge, UB8 3PH, United Kingdom; E-Mail: Evelyne.ElMasri@brunel.ac.uk
2. TWI Ltd, Cambridge, Cambridgeshire, CB21 6AL, United Kingdom; E-Mail: Tat-Hean.Gan@brunel.ac.uk

* **Correspondence:** Evelyne El Masri; E-Mail: Evelyne.ElMasri@brunel.ac.uk

Academic Editor: Luciano Ombres

Special Issue: Fiber Composite Materials and Civil Engineering Applications

Recent Progress in Materials
2020, volume 2, issue 3
doi:10.21926/rpm.2003020

Received: May 28, 2020
Accepted: August 17, 2020
Published: August 26, 2020

Abstract

Carbon fibre reinforced polymer (CFRP) systems as sheets or plates are commonly used to strengthen and retrofit damaged reinforced concrete beams. In general, the bond between the FRP element and concrete defines the effectiveness of the externally bonded FRP materials. In most cases, the interface bonding behaviour is usually tested via static loading conditions. In this paper, the bonding is verified under dynamic conditions. Wave propagation is modelled in delaminated CFRP strengthened reinforced concrete beam. First, the Wave Finite Element (WFE) is applied to predict the wave characteristics of the waveguides. Having established free wave solutions, one can couple it to a damaged segment that can be modelled in FE. The bond–slip model is used to simulate the CFRP to concrete interface bonding behaviour. Then, wave scattering characteristics are identified at the damaged section. Partial loss of debonding results in high refection coefficient of higher order modes. This study can lead to further advance based damage detection techniques related to debonding of FRP element to concrete with no required access to the FRP lamina.

Keywords
CFRP; concrete; debonding; damage detection; guided waves; wave-based method; WFE; scattering.

1. Introduction

Fibre-reinforced polymer (FRP) is excessively used in advanced concrete applications due to their superior performance compared to the typical steel reinforcements. In particular, FRP system can be externally bonded for strengthening of reinforced concrete (RC) beams [1]. FRP-strengthened RC structural members demonstrate improved flexural strength, shear and torsional capability, seismic resilience and durability [2]. Furthermore, retrofitting of damaged RC beam with FRP composites is widely applied since they provide non-corrosive properties, stiffness, strong structural tensile strength, ease of installation and chemical attack protection [3]. In addition, CFRP features the most strength amongst FRP composites with variety of strength range [4].

When it comes to structural behaviour of CFRP-strengthened RC beams, the performance does not rely solely on the materials such as concrete, steel and FRP lamina. However, the bonding behaviour between concrete and CFRP lamina plays a significant role since it defines the stress transfer from concrete to the CFRP [5]. Subsequently, debonding damage detection of the CFRP-strengthened RC beams is essential to maintain the integrity and structural performance of the structure. There are several techniques that reported the detection of debonding between concrete and CFRP lamina.

The behaviour of bonding between concrete surface and lamina had been investigated in literature. For instance, the bonding behaviour between Steel Reinforced Polymer (SRP) and concrete surface were investigated experimentally by taking into account the effect of the concrete surface roughness in the bonded region, the density of the steel fabric, the ratio of the epoxy covered concrete surface width to the SRP strip width and the length of the bonded interface [6]. Furthermore, the SRP-concrete interfacial bonding behaviour and strength were successfully modelled and calibrated by using an experimental database [7]. Regarding FRP-retrofitted RC beams, the full nonlinear moment-curvature relationship undergoing interfacial slip is presented in [8]. where debonding is evaluated via cohesive interface. Results have shown very close agreement between the computed values and experimental results. On the other hand, a nonlinear semi-analytical model was developed to predict debonding of FRP-concrete interface in RC beams subjected to concentrated or uniform loads. The model employed second order differential equations with their dependent variables being the strain in the FRP and the relative normal displacement of the interface. Satisfactory agreement was found between model and experimental results [9].

In order to detect the debonding between the concrete and CFRP lamina, microwave imaging method was adopted based on near-filed approach of two-dimensional images of the structure [10]. By monitoring the air-filled debonding in FRP-strengthened reinforced concrete via infrared thermography, debonding between concrete and FRP can be detected in bridge decks [11] and CFRP RC beams [12]. In addition, far-field radar method was applied to detect interfacial defects in

an FRP wrapped concrete member through merging synthetic aperture radar measurements with back projection algorithms [13]. Furthermore, acoustic emission was used to detect the debonding between concrete and CFRP lamina using different approaches: applying parametric intensity principal component analysis [14], exciting the structure and using a laser beam to identify the vibration response [15]. Also, impact-echo method was employed to detect the debonding at the interface between concrete and CFRP [16].

The piezoelectric transducers (PZT) were employed excessively in detecting the bond defect between concrete and FRP. For example, a surface mounted PZT was used as an actuator and an embedded PZT as a sensor to detect debonding between concrete and CFRP [17]. In addition, guided wave techniques using embedded PZT in the structure was used to detect the interfacial defects [18]. Furthermore, spectral model was developed on similar model via simulation and experimental validation [19].

Despite the fact the acoustic emission, ultrasonic detection, infrared thermography, electrochemical impedance spectroscopy and PZT methods can successfully detect the bond defect between concrete and CFRP, few of them have been implemented successfully to interfacial damage monitoring [20]. Moreover, the guided wave techniques described above require embedded PZTs inside the structure which require special interrogation and preparation [21]. In addition, some of the mentioned techniques involve access to the FRP lamina. This put some limitations into the applications of those techniques on real structure where the bottom of the beam might be inaccessible due to partitions.

In this paper, detection of debonding between concrete and CFRP lamina is investigated using guided waves characteristics. The latter are defined first in undamaged beam section via the application of the Wave Finite Element (WFE). The model features full bonding between concrete and CFRP composite. Then, the defined waves solutions are coupled to the damage section that is modelled in FE. The damage features partial loss of the bond–slip model to simulate the CFRP to concrete interface behaviour with defect. Next, wave scattering characteristics are calculated. Finally, conclusions relate to additional future works corresponding to damage detection techniques of debonding of CFRP element to concrete.

2. Materials and Methods

2.1 WFE formulation

The dynamic response of simple structures such as rods and beams can be computed analytically. However, the solution is not straightforward for complicated structures. Usually, one tends to modelling solution such as full or partial finite element analysis (FEA). However, this imposes computational cost, time, and accuracy errors for complex models especially at high frequencies. An alternative approach is the wave-based method. To analyse a waveguide, one approach is the spectral finite element (SFE). However, this requires new spectral mass and stiffness matrices for each scenario on a case-by-case basis [22].

Alternatively, the Wave Finite Element method (WFE) can be employed of a small segment of the waveguide modelled in FE. The WFE method forecasts the wave characteristics of a short periodic waveguide through expressing the continuity of displacements and equilibrium of forces at the boundaries between consecutive segments. Then, an eigenvalue problem is formulated in

terms of a transfer function across the section. The solutions as eigenvalues relate the variables, as function of the wavenumbers of the waveguide, associated with the right and left sides of the section. Furthermore, the eigenvectors are related with the displacements and forces on the cross section. This eigenvalue problem is solved at each step frequency [23].

The dynamic stiffness matrix is established using the mass and stiffness matrices. Here, ANSYS is employed to model the CFRP-strengthened RC waveguide section in order to extract the required matrices. After the latter is accomplished, the dynamic stiffness matrix is deployed to formulate the transfer matrix. Next, the eigenvalue problem is solved at each step frequency to acquire the wavenumbers and wave mode shapes.

Relating the element nodal displacements and forces, the dynamic stiffness matrix at frequency ω of a finite section is defined by

$$\mathbf{D} = \mathbf{K} - \omega^2 \mathbf{M} \tag{1}$$

where $\mathbf{K}$ and $\mathbf{M}$ are the $n \times n$ stiffness and mass matrices of the waveguide section, where n is the total number of DOFs. As in Figure 1, L and R denote the left and right sides and Δ is the length of the section modelled of the waveguide. Δ should not be too large with respect to the shortest wavelength to reduce discretization errors, nor too small to avoid round off-errors [24].

The dynamic stiffness matrix is partitioned accordingly as,

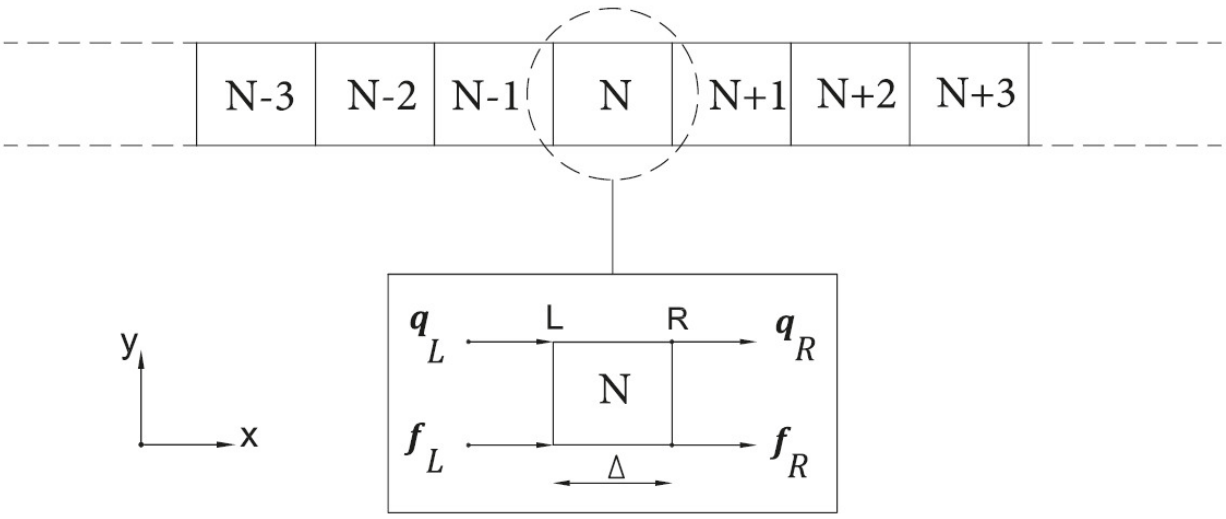

Figure 1 Structure with periodic elements where the cell N of length Δ is shown with the force and displacement vectors on the right and left-hand sides.

$$\begin{bmatrix} \boldsymbol{D}_{LL} & \boldsymbol{D}_{LR} \\ \boldsymbol{D}_{RL} & \boldsymbol{D}_{RR} \end{bmatrix} \begin{bmatrix} \boldsymbol{q}_L \\ \boldsymbol{q}_R \end{bmatrix} = \begin{bmatrix} \boldsymbol{f}_L \\ \boldsymbol{f}_R \end{bmatrix} \tag{2}$$

The propagation constant $\lambda = e^{-ik\Delta}$ relates the right and left displacement and forces with k as the wavenumber such as the periodic conditions for the displacements and the equilibrium condition at the junction of the two elements are $\boldsymbol{q}_R = \lambda \boldsymbol{q}_L$ and $\boldsymbol{f}_R = -\lambda \boldsymbol{f}_L$. Subsequently, Eq. (2) can be written as

$$\mathbf{T}\begin{Bmatrix}\boldsymbol{q}_L\\ \boldsymbol{f}_L\end{Bmatrix} = \lambda\begin{Bmatrix}\boldsymbol{q}_L\\ \boldsymbol{f}_L\end{Bmatrix} \tag{3}$$

where $\mathbf{T}$ is the transfer function that features continuity of displacements $\boldsymbol{q}$ and equilibrium of forces $\boldsymbol{f}$ between the boundaries of two consecutive elements [23]. Then,

$$\mathbf{T} = \begin{bmatrix} -\boldsymbol{D}_{LR}^{-1}\boldsymbol{D}_{LL} & \boldsymbol{D}_{LR}^{-1} \\ -\boldsymbol{D}_{RL} + \boldsymbol{D}_{RR}\boldsymbol{D}_{LR}^{-1}\boldsymbol{D}_{LL} & -\boldsymbol{D}_{RR}\boldsymbol{D}_{LR}^{-1} \end{bmatrix} \tag{4}$$

The eigenvalue problem presented by the transfer matrix is solved at each frequency step where the wavenumbers k are obtained from the eigenvalues. A good practice is to cluster the solutions into positive and negative going waves. The former are characterised by $\left|\lambda_j^+\right| < 1$ and the latter by $\left|\lambda_j^+\right| > 1$. For $\left|\lambda_j^+\right| = 1$, the associated waves are considered positive going if they accomplish the condition of $Re\{\boldsymbol{f}_L^H\dot{\boldsymbol{q}}_L\} = Re\{i\omega\boldsymbol{f}_L^H\boldsymbol{q}_{fL}\} < 0$

Similarly, regarding wave modes of the right eigenvectors in Eq. (3), one can group those into positive and negative going waves such as

$$\boldsymbol{\Phi}^+ = [\boldsymbol{\Phi}_1^+ \cdots \boldsymbol{\Phi}_n^+]; \boldsymbol{\Phi}^- = [\boldsymbol{\Phi}_1^- \cdots \boldsymbol{\Phi}_n^-]; \boldsymbol{\Phi} = [\boldsymbol{\Phi}^+\boldsymbol{\Phi}^-] \tag{5}$$

where each wavemode is divided into displacement $\boldsymbol{q}$ and force $\boldsymbol{f}$ sub-vectors,

$$\boldsymbol{\Phi}_j = \begin{Bmatrix}\boldsymbol{\Phi}_q\\ \boldsymbol{\Phi}_f\end{Bmatrix}_j \tag{6}$$

The left eigenvectors of the transfer matrix $\mathbf{T}$ can be obtained as well,

$$\boldsymbol{\Psi}_j = \{\boldsymbol{\Psi}_f\boldsymbol{\Psi}_q\}_j; \boldsymbol{\Psi}^{\pm} = \begin{bmatrix}\boldsymbol{\Psi}_1^{\pm}\\ \cdots \\ \boldsymbol{\Psi}_N^{\pm}\end{bmatrix}; \boldsymbol{\Psi} = \begin{bmatrix}\boldsymbol{\Psi}^+\\ \boldsymbol{\Psi}^-\end{bmatrix} \tag{7}$$

Since the left and right wavemodes are orthogonal, they can be normalised such as

$$\boldsymbol{\Psi}^+\boldsymbol{\Phi}^+ = \mathbf{I} \tag{8}$$

The main advantage if the above normalisation is to improve the conditioning of the matrices that require to be inverted [24]. This is achieved by multiplying the anticipated matrix by the normalised right eigenvectors.

In addition, the relation between the physical domain (where the motion is described in terms of q and f), and the wave domain (described in terms of waves amplitudes such as $\mathbf{a}^+$ and $\mathbf{a}^-$ as the positive and negative going waves) is expressed via

$$\begin{Bmatrix}\boldsymbol{q}_L\\ \boldsymbol{f}_L\end{Bmatrix} = \begin{bmatrix}\boldsymbol{\Phi}_q^+ & \boldsymbol{\Phi}_q^- \\ \boldsymbol{\Phi}_f^+ & \boldsymbol{\Phi}_f^-\end{bmatrix}\begin{Bmatrix}\mathbf{a}^+\\ \mathbf{a}^-\end{Bmatrix} \tag{9}$$

2.2 CFRP-Strengthened RC Beams Modelling in FE

A prior step to apply WFE method to the undamaged CFRP-strengthened RC Beam, a section should be modelled in FE. Here, ANSYS was used for this application in order to extract the associated mass and stiffness matrices. Four different types of elements were used to model the associated section: solid element for concrete and adhesive, embedded secrete element for reinforcement rebars, shell element for CFRP lamina and interface element for interface interaction as illustrated in Figure 2. First, the modelling elements are described. Then, the material properties and bonding model are presented.

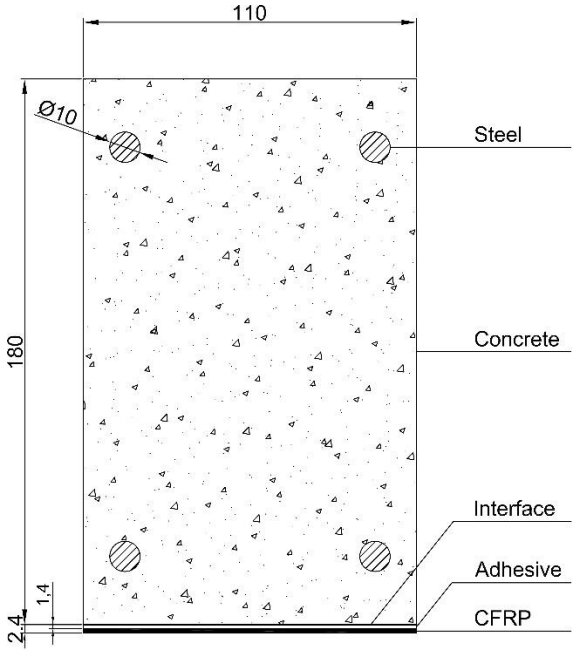

Figure 2 Cross Section of CFRP-strengthened RC beam to be modelled in FE.

SOLID65 [25] was used to model concrete. It is a 3D solid element with three DOFs, which are translations in the X, Y and Z directions, and it is defined by eight nodes. This element can simulate cracking under tension in three orthogonal directions, crushing under compression, plastic deformation and creep. Reinforcement rebars were modelled via the 3D discrete element REINF264 [25] embedded in the SOLID65 element [26]. The nodal locations, degrees of freedom and connectivity of the REINF264 element are identical to those of the base element which is the SOLID65. The location of the rebar was defined as an offset distance from the edges of the base element selected (i.e. SOLID65). The main advantages using REINF264 as embedded reinforcement are associated with no need to model the bonding behaviour between the steel reinforcement and surrounding concrete elements, and no extra mesh/nodes is required to identify the rebar element.

CFRP was modelled via the SHELL181 element [25]. Shell element was always favoured to model FRP lamina since the thickness is relatively small compared to the structure, no additional nodes were required and the aspect ratio of the element did not exceed the acceptable limit [27]. SHELL181 is a four nodes element with six degrees of freedom such as translations and rotations about X, Y and Z directions. In this model, the membrane option was only used the therefore each node of SHELL181 had only the translation DOFs in X, Y and Z directions.

SOLID45[25] element was used to model the adhesive. It is a 3D solid element with three DOFs, which are translations in the X, Y and Z directions, and it is defined by eight nodes. The element has plasticity, creep, swelling, stress stiffening, large deflection and large strain capabilities. The element comprises two sets of nodes. In this model, one set was applied with the interface element and the other with the CFRP [28].

The bonding behaviour between the CFRP and adjacent concrete surfaces was modelled using the cohesive element INTER205[25] between the top surface of the adhesive and bottom surface of the concrete. INTER205 is a 3D eight nodes with DOFs as translations in the X, Y and Z directions. It is a linear interface element that is able of simulating various interfaces between two surfaces as well as delamination progression. In principle, the debonding occurred when initially coincident nodes experience an increase in longitudinal or transversal displacement [29].

The CFRP-strengthened RC Beam section was modelled using the dimensions and meshing as shown in Figure 3. The length Δ of the segment in the X direction was equal to 0.01 m, the total number of DOFs n is 210, and a hysteretic damping value η of 0.004 was chosen. The CFRP plate had a thickness and width of 1.4 mm. A layer of Sikadur 30 LP having a thickness of 1 mm was used to simulate the adhesive [29]. Material properties are summarised in Table 1. One started by modelling the concrete element with designated mesh. Then, the embedded reinforcement were assigned to the corner concrete elements. CFRP elements were modelled with the adhesive ones on top. Both concrete bottom surface nodes and adhesive top surface nodes shared adjacent nodes where the interface elements are assigned.

Table 1 Material properties required for the FE model.

Material	Type	Modulus of Elasticity (GPa)	Poisson Ratio	Density (kg/m^3)	Shear Modulus (GPa)
Concrete	Isotropic	25	0.2	2400	-
Steel	Isotropic	200	0.3	7850	-
CFRP	Orthotropic	E_x=160, $E_{y,z}$=16	$V_{xy,xz}$=0.28, V_{yz}=0.42	1800	$G_{xy,yz}$=7
Adhesive	Isotropic	10	0.32	1650	-

For composite lamina modeled as layer system, delamination can be represented as a reduction of the resultant Modulus of Elasticity of the lamina of a specific layer number and over a certain distance. This results in lower bending stiffness and frequency predictions. As seen in [30], the proposed delamination modeling technique had shown robust results in comparison to experimental data especially at structural boundaries.However, in the proposed problem, the delamination occurs at the interface between concrete and CFRP. Therefore, the bond-slip model selected employed the INTER205 element to simulate the bonding/debonding at the CFRP-concrete interface. The cohesive zone material option was used for the interface element. In specific, the exponential form as bond-slip model was adapted as presented in [31]. In principal, the exponential model was initiated with an increasing segment up to the ultimate shear stress τ_u with slip s_u. Next, a softening response up to the ultimate attained slip equivalent to 4×s_u. The correspondent equations are presented in [32] as

$$\tau = \tau_{max}\left(\frac{s}{s_0}\right)\left[\frac{3}{2+\left(\frac{s}{s_0}\right)^3}\right] \tag{10}$$

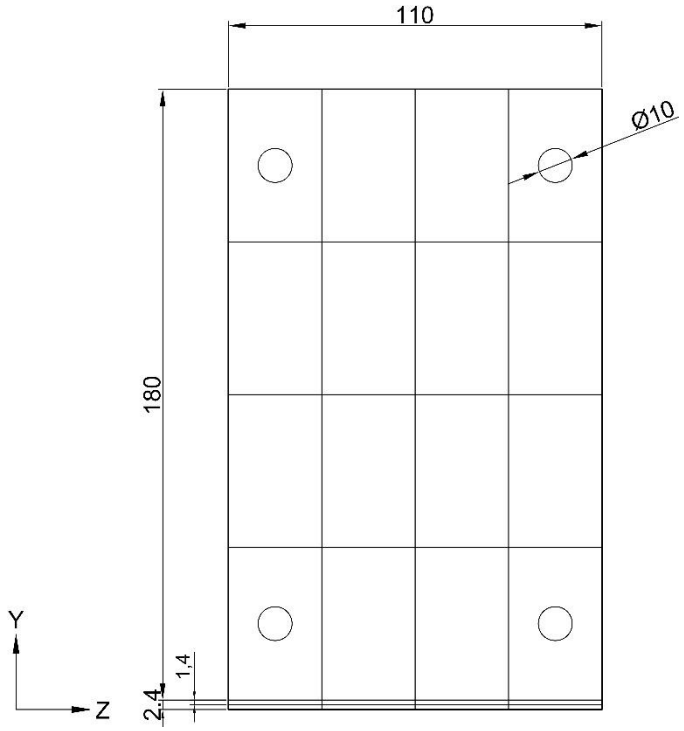

Figure 3 FE mesh of CFRP-strengthened RC Beam. Dimensions are in mm.

where $\tau_{max} = 3.5\ {f_c'}^{0.19}$ with f_c' the compressive strength of concrete, s_0 = 0.065 mm and s is the slip between the concrete and CFRP interfaces.

To better understand the effect of CFRP-concrete debonding on the wave solutions, a small damaged section of the waveguide was modelled as well in FE in order to extract the associated matrices to apply the WFE solutions and compared it to the undamaged ones. The damaged section was modelled with similar dimensions and materials properties of the undamaged one. However, the partial loss of bonding between CFRP and concrete in the damaged section was reflected via a reduction of 60% in the value of the ultimate shear stress associated with the interface element in Eq. (10).

After the FE model was complete, one could extract the associated stiffness and mass matrices. Here, a convergence test was not required since one was only interested in extracting the required stiffness and mass matrices. However, to check the model features and mesh precision, a convergence test was conducted in [33]. In addition, the elements and mesh size should satisfy the following condition to reduce errors in wave solutions [34].

$$l_{y,z} < \frac{\lambda_{min}}{2}; \lambda_{min} = \frac{2\pi}{k_{max}} \tag{11}$$

where $l_{y,z}$ is the element size in Y and Z direction, λ_{min} is the minimum wave length associated with the maximum wavenumber k_{max} within a defined frequency range. Here, k_{max} value is 50

rad/m which provides a value of λ_{min} equivalent to 125.6 mm. Then, $l_{y,z}$ is recommended to be less than 63 mm. All sides of the model cross section in Y and Z direction are less than the recommended value.

An eigenvalue problem was then formed for each model (damaged and undamaged) at each step frequency, where the eigenvalues relate to wavenumber solutions of right and left propagating waves, and the eigenvectors to the associated force and displacement wave mode shapes.

2.3 Coupling of Waveguides

Scattering of incidents waves can be associated with the presence of damage or discontinuity. Therefore one can consider the scattering due to discontinuity of a finite length through coupling of a finite damage section to undamaged waveguides as illustrated in Figure 4. This coupling approach is noted as the WFE-FE-WFE [35]. Here, the damaged section is modelled in FE with 60% in the value of the ultimate shear stress associated with the interface element, and with a finite length h = 0.05m including a segment length of Δ_i = 0.01 m. Then, the finite damaged length in connected at the ends to the undamaged waveguides modelled in WFE as in Section 2.1. The mesh considers that both interfaces are compatible since they share same nodal coordinates and DOFs.

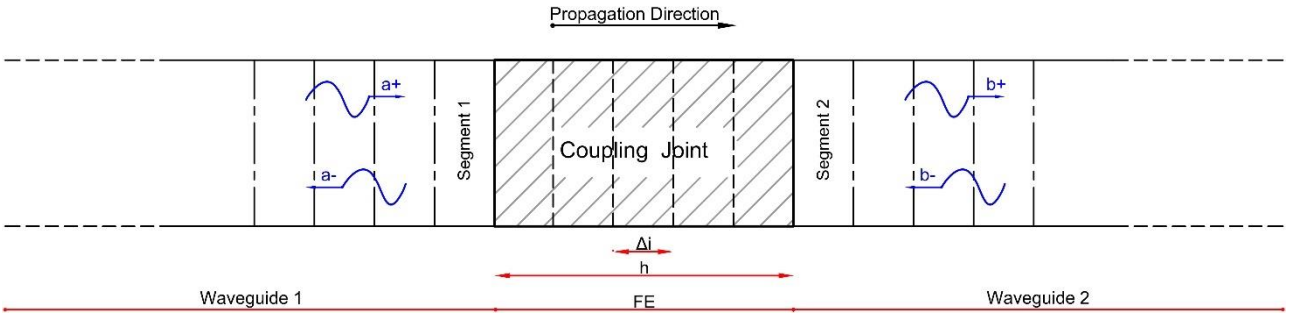

Figure 4 The interface between the WFE segments 1 and 2 connected to the FE model of the coupling joint as the damage waveguide.

Considering $\mathbf{D}_c$ as the dynamic stiffness matrix of the coupling joint that can be expressed in terms of its mass and stiffness matrices as $\mathbf{M}_c$ and $\mathbf{K}_c$ respectively as

$$\mathbf{D}_c = \mathbf{K}_c - \omega^2 \mathbf{M}_c \tag{12}$$

For the coupling joint, the left and right interface nodes are denoted by l and $r$respectively. The internal nodes are expressed by i. D_c is written as

$$\mathbf{D}_c = \begin{bmatrix} \mathbf{D}_{ll} & \mathbf{D}_{li} & \mathbf{D}_{lr} \\ \mathbf{D}_{il} & \mathbf{D}_{ii} & \mathbf{D}_{ir} \\ \mathbf{D}_{rl} & \mathbf{D}_{ri} & \mathbf{D}_{rr} \end{bmatrix} \tag{13}$$

By applying the dynamic condensation presented in [24], the dynamic stiffness matrix $\mathbf{D}_c$ can be condensed to its internal DOFs. This is given by

$$\mathbf{D}_c^* = \begin{bmatrix} \mathbf{D}_{ll} - \mathbf{D}_{li}\mathbf{D}_{ii}^{-1}\mathbf{D}_{il} & \mathbf{D}_{lr} - \mathbf{D}_{li}\mathbf{D}_{ii}^{-1}\mathbf{D}_{ir} \\ \mathbf{D}_{rl} - \mathbf{D}_{ri}\mathbf{D}_{ii}^{-1}\mathbf{D}_{il} & \mathbf{D}_{rr} - \mathbf{D}_{ri}\mathbf{D}_{ii}^{-1}\mathbf{D}_{ir} \end{bmatrix} \tag{14}$$

The displacement and forces at the end of the coupling joint can be related such as

$$\mathbf{D}_c^* \begin{Bmatrix} \boldsymbol{q}_l^c \\ \boldsymbol{q}_r^c \end{Bmatrix} = \begin{Bmatrix} \boldsymbol{f}_l^c \\ \boldsymbol{f}_r^c \end{Bmatrix} \tag{15}$$

Segments 1 and 2 of waveguides 1 and 2 are modelled in WFE. Consider a^+ and b^- the amplitudes of the waves incidents on the coupling joint interface. Let a^- and b^+ the amplitudes of the waves reflect by the coupling joint interface. By implementing Eq. (9), one can write the following for waveguides 1 and 2

$$\begin{Bmatrix} q_r^1 \\ q_l^2 \\ f_r^1 \\ f_l^2 \end{Bmatrix} = \begin{bmatrix} \boldsymbol{\Phi}_{q_1}^+ & 0 & \boldsymbol{\Phi}_{q_1}^- & 0 \\ 0 & \boldsymbol{\Phi}_{q_2}^+ & 0 & \boldsymbol{\Phi}_{q_2}^- \\ \boldsymbol{\Phi}_{f_1}^+ & 0 & \boldsymbol{\Phi}_{f_1}^- & 0 \\ 0 & \boldsymbol{\Phi}_{f_2}^+ & 0 & \boldsymbol{\Phi}_{f_2}^- \end{bmatrix} \begin{Bmatrix} a^+ \\ b^- \\ a^- \\ b^+ \end{Bmatrix} \tag{16}$$

After the application of WFE, $\boldsymbol{\Phi}_{q,f}^+$ and $\boldsymbol{\Phi}_{q,f}^-$ are identified by concatenating the relevant vectors for waveguides 1 and 2 as

$$\boldsymbol{\Phi}_q^{inc} = \begin{pmatrix} \boldsymbol{\Phi}_{q_1}^+ & 0 \\ 0 & \boldsymbol{\Phi}_{q_2}^+ \end{pmatrix} \; \boldsymbol{\Phi}_q^{ref} = \begin{pmatrix} \boldsymbol{\Phi}_{q_1}^- & 0 \\ 0 & \boldsymbol{\Phi}_{q_2}^- \end{pmatrix} \; \boldsymbol{\Phi}_f^{inc} = \begin{pmatrix} \boldsymbol{\Phi}_{f_1}^+ & 0 \\ 0 & \boldsymbol{\Phi}_{f_2}^+ \end{pmatrix} \; \boldsymbol{\Phi}_f^{ref} = \begin{pmatrix} \boldsymbol{\Phi}_{f_1}^- & 0 \\ 0 & \boldsymbol{\Phi}_{f_2}^- \end{pmatrix} \tag{17}$$

By applying the continuity and force equilibrium conditions, the nodal DOFs and forces at the interfaces are equal to those of the undamaged waveguides on each side

$$\begin{pmatrix} \boldsymbol{q}_l^c \\ \boldsymbol{q}_r^c \end{pmatrix} = \begin{pmatrix} \boldsymbol{q}_r^1 \\ \boldsymbol{q}_l^2 \end{pmatrix} \; \begin{pmatrix} \boldsymbol{f}_l^c \\ \boldsymbol{f}_r^c \end{pmatrix} = \begin{pmatrix} \boldsymbol{f}_r^1 \\ \boldsymbol{f}_l^2 \end{pmatrix} \tag{18}$$

Then, the scattering matrix $\mathbf{S}$ is expressed as

$$\begin{pmatrix} \boldsymbol{a}^+ \\ \boldsymbol{b}^- \end{pmatrix} = \mathrm{S} \begin{pmatrix} \boldsymbol{a}^- \\ \boldsymbol{b}^+ \end{pmatrix} \tag{19}$$

After combining Eq. (15) to Eq. (18), one can write

$$\mathbf{S} = -\left(-\mathbf{D}_c^* \boldsymbol{\Phi}_q^{ref} + \boldsymbol{\Phi}_f^{ref}\right)^{-1} \left(-\mathbf{D}_c^* \boldsymbol{\Phi}_q^{inc} + \boldsymbol{\Phi}_f^{inc}\right) \tag{20}$$

It is worth noticing that the scattering matrix S is a block matrix where the diagonal matrices comprise the reflection coefficients, and the off-diagonal matrices contain the transmission coefficients. If a reduced number of waves is retained, then the matrix to be inverted in Eq. (20) is not square and pseudo-inversion is required [35]. Using $\boldsymbol{\Psi}$ in Eq. (7) and the orthogonality condition in Eq. (8), one can reduce the numerical errors. This is achieved by premultiplying Eq. (20) with the matrix $\boldsymbol{\Psi}_q^{ref}$ such as

$$\boldsymbol{\Psi}_q^{ref} = \begin{bmatrix} \boldsymbol{\Psi}_{q_1}^- & 0 \\ 0 & \boldsymbol{\Psi}_{q_2}^- \end{bmatrix} \tag{21}$$

Therefore, the scattering matrix $\mathbf{S}$ becomes

$$\mathbf{S} = -\boldsymbol{\Psi}_q^{ref}\left(-\mathbf{D}_c^*\boldsymbol{\Phi}_q^{ref} + \boldsymbol{\Phi}_f^{ref}\right)^{-1}\boldsymbol{\Psi}_q^{ref}\left(-\mathbf{D}_c^*\boldsymbol{\Phi}_q^{inc} + \boldsymbol{\Phi}_f^{inc}\right) \tag{22}$$

3. Results

3.1 Wave Solutions of CFRP-Strengthened RC Beam

After the application of WFE on the CFRP-strengthened RC beam section, one can calculate the associated wavenumbers and nodal solutions as displacements and forces. For each model, there are 210 different wavenumbers in accordance with number of DOFs, but a large number of them have a significant imaginary part matching to highly attenuated waves. Subsequently, the latter need to be eliminated. In this model, only the wave modes are only retained, at each frequency step, if they fulfil the condition $|Im(\mathrm{k}\Delta)| \leq 0.3$. This is equivalent to 10 dB along the element length in the direction of propagation.

The dispersion curves relating to the least attenuated waves are plotted for both damaged and undamaged waveguides. These can be divided into three categories based on the variation of the real and imaginary part of the associated wavenumbers across the frequency range. In Figure 5, propagating or zero order modes dispersion curve is plotted. They are the wave modes that can propagate all over the frequency range with zero imaginary part of the wavenumber. Normalised modal displacement of propagating wave modes in the undamaged waveguides at 2000 Hz are plotted in Figure 6 in the direction of the major displacement.

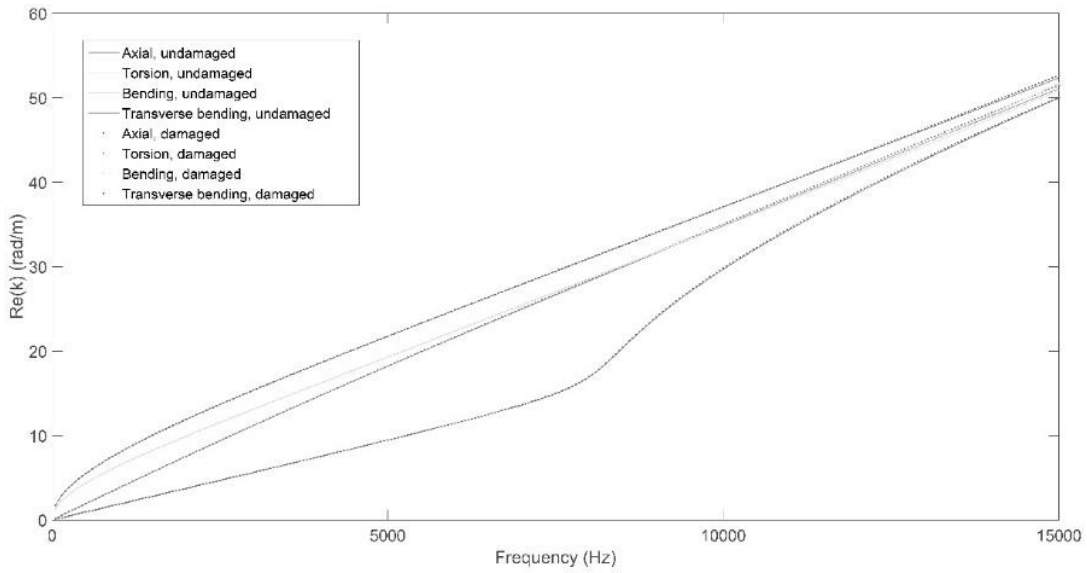

Figure 5 Dispersion curves for the real part of the wavenumbers for propagating wave modes in CFRP-strengthened RC beam.

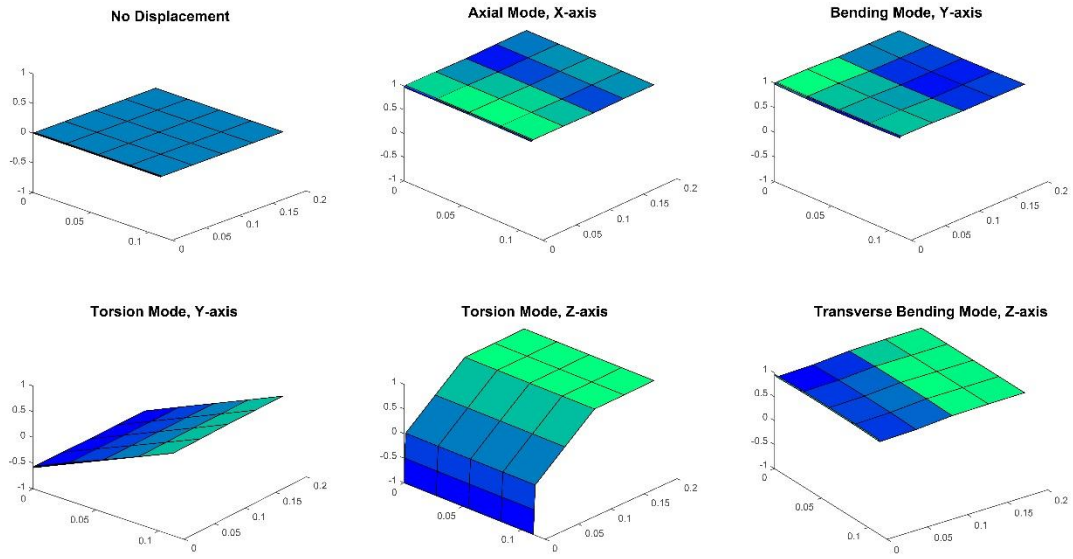

Figure 6 Nodal displacement of the undamaged cross section for the propagating modes in the direction of the major displacement at 2000 Hz.

In Figure 7, dispersion curve of evanescent modes in damaged and undamaged waveguides is plotted. They are the modes with purely imaginary wavenumbers before their cut-on frequency as denoted as "E" in the caption. In Figure 8, the complex modes wavenumbers are illustrated for both damaged and undamaged waveguides. They are the modes with complex wavenumbers before their cut-on frequency as denoted as "C" in the caption. Above cut-on, the wavenumber becomes purely real for both evanescent and complex modes. Figure 9 and Figure 10 show the normalised modal displacement of evanescent and complex wave modes, respectively, at their cut-on frequency in the direction of major displacement.

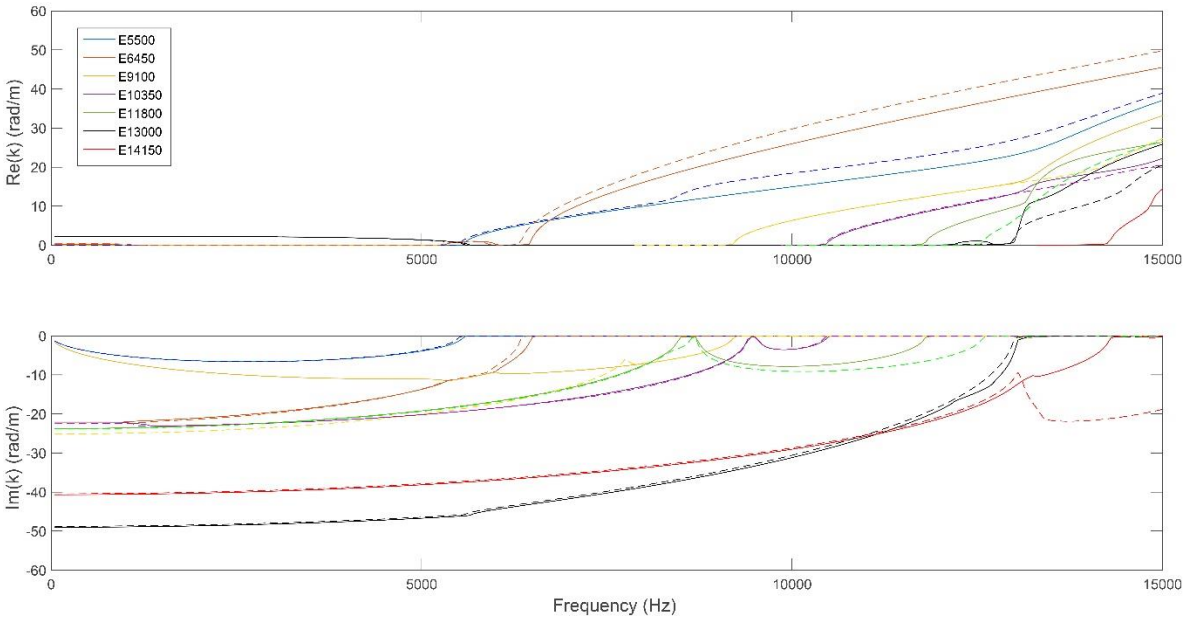

Figure 7 Dispersion curves for the evanescent wave modes of CFRP-strengthened RC beam: – undamaged section, - - - damaged section. "E" denotes an evanescent wave with its associated cut-on frequency in Hz.

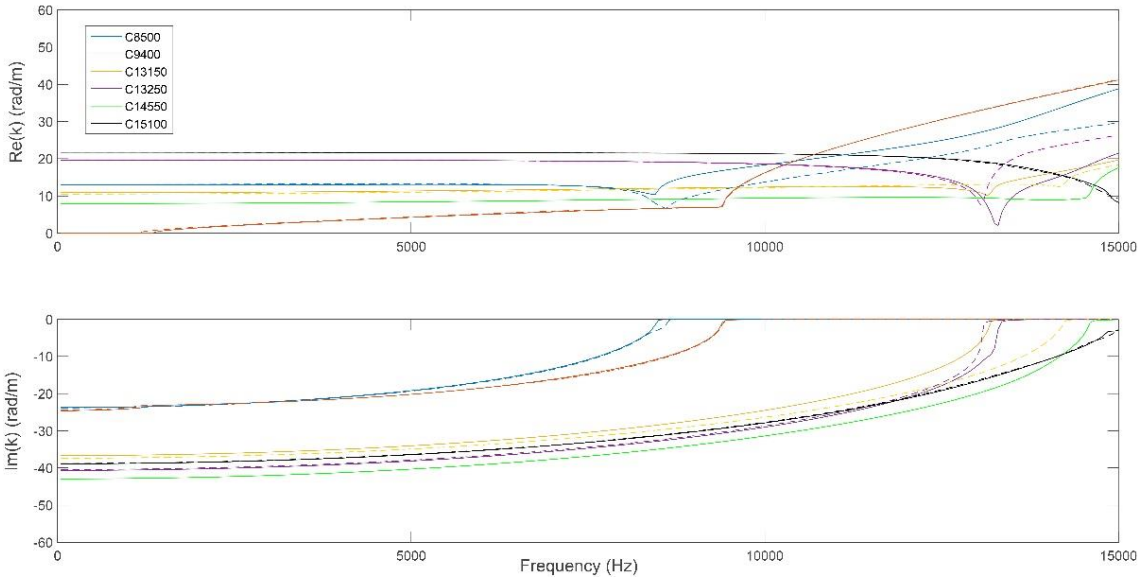

Figure 8 Dispersion curves for the complex wave modes of CFRP-strengthened RC beam: – undamaged section, - - - damaged section. "E" denotes an evanescent wave with its associated cut-on frequency in Hz.

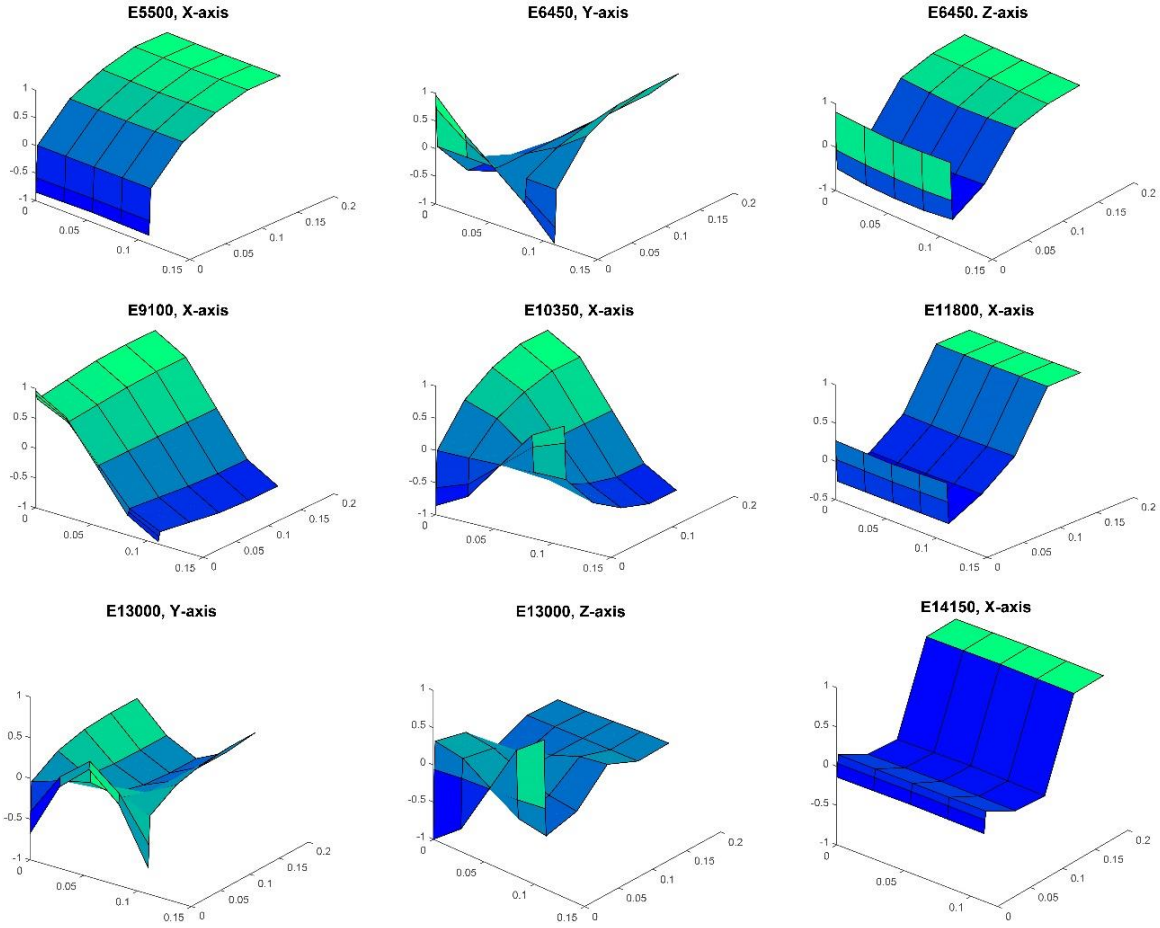

Figure 9 Nodal displacement of the undamaged cross section for the evanescent modes in the direction of the major displacement at their associated cut-on frequency.

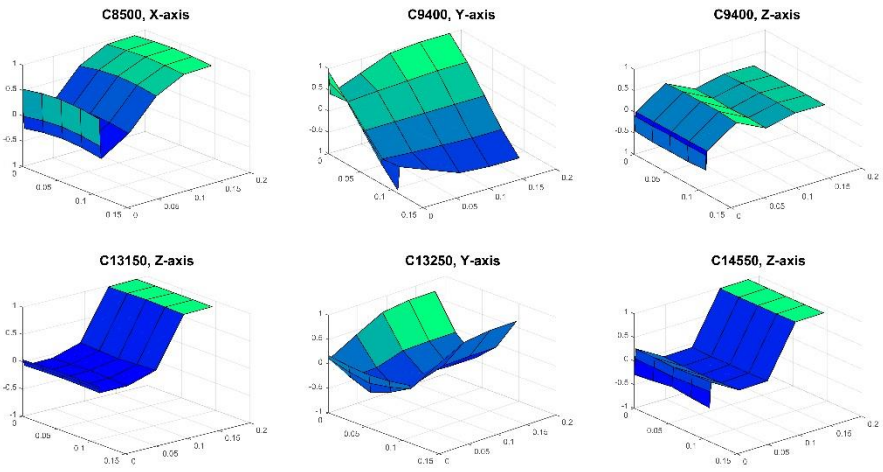

Figure 10 Nodal displacement of the undamaged cross section for the complex modes in the direction of the major displacement at their associated cut-on frequency.

3.2 Scattering Properties due to Concrete-CFRP Debonding

The WFE-FE-WFE approach is applied. The scattering matrix $\mathbf{S}$ is computed at each step frequency. The high attenuated modes having a high imaginary part are eliminated. In Figure 11, the magnitudes of the reflection coefficients for the least attenuated waves due to loss of bonding between CFRP and concrete are plotted.

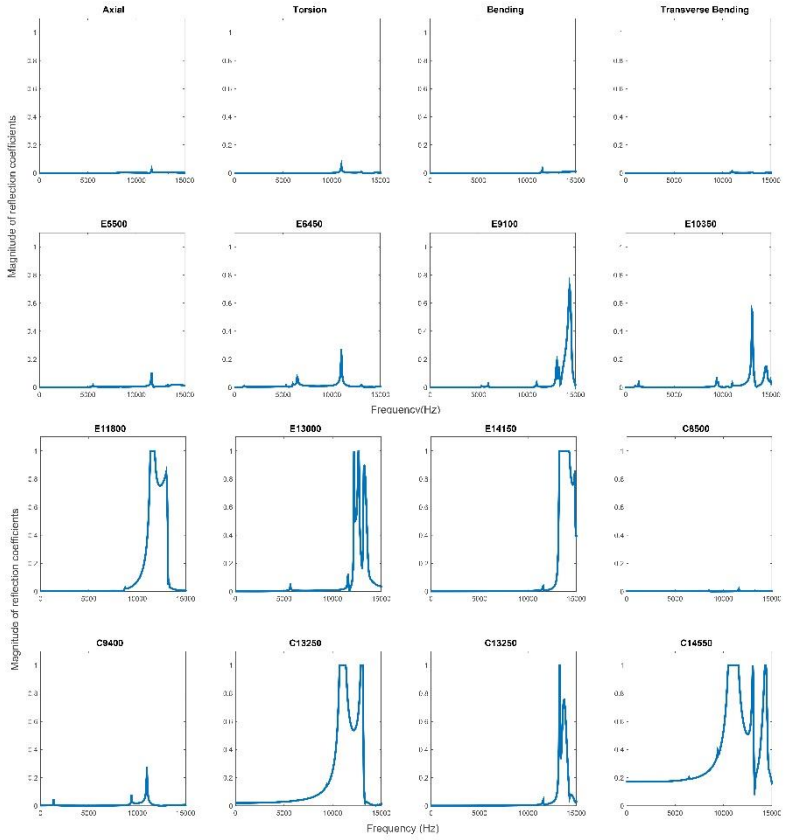

Figure 11 Magnitude of the reflection coefficients for the least attenuated modes in CFRP-strengthened RC beam due to 60\% loss in interface bonding between CFRP and concrete over a length of 0.05m.

4. Discussion

Partial debonding of the interface between CFRP and concrete has resulted in some clear differences in the wave properties between damaged and undamaged waveguides. Those differences and associated reasons are highlighted in this section.

In Figure 5, there is only a slight difference between the wavenumbers of propagating waves of the damaged and undamaged waveguides. This is due to the fact that these wave modes as illustrated in Figure 6 are mainly governed by the concrete structural stiffness rather by the CFRP-concrete bonding. This results in a negligible magnitudes of reflection coefficients associated with propagating wave modes shown in Figure 11. This means that propagating waves as axial, torsion, bending and transverse bending are not sensitive to the debonding of the interface between CFRP and concrete.

On the other hand, partial debonding of the interface between CFRP and concrete causes changes in the evanescent and complex wave modes wavenumbers as illustrated in Figure 7 and Figure 8 respectively. One can notice the shift in the cut-on frequencies between the two models associated with E6450, E11800, E14150, C8500, C13150, C13250 and C14550. In addition, changes in the wavenumbers away from the cut-on frequencies are seen with the wave modes E6450, E550 and E13000. Those wave modes have shown cross sectional displacement as illustrated near their cut-on in Figure 9 and Figure 10 for evanescent and complex modes respectively. For each of the mentioned wave modes, the nodes associated with the interface CFRP-concrete location have distinguished displacement compared to the whole cross section deformed shape. For instance, E11800 shows a different bending around the interface nodal displacement, and E13000 displays a torsional behaviour around the same location that is different from the other nodes deformed shapes within the same wave mode. Therefore, some of these wave modes had shown a sensitivity toward the partial loss of the bonding between CFRP and concrete resulting in high magnitude of reflection coefficients in Figure 11.

Here, the wave modes that have shown a magnitude of reflection coefficients due to debonding higher than 0.5 are selected. Those are plotted in Figure 12 and Figure 13 with their associated wavenumbers for damaged and undamaged waveguides. Vertical lines are applied to indicate the frequencies at which the selected wave modes have demonstrated a peak in the magnitude of reflection coefficients that are explained here.

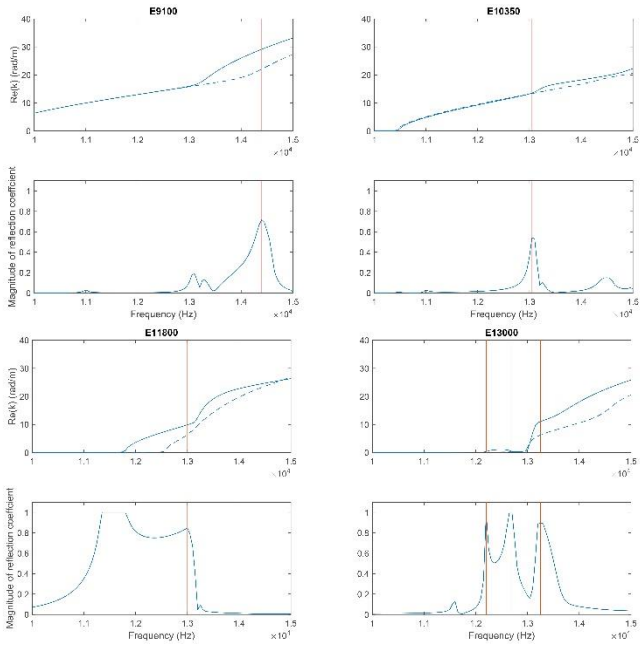

Figure 12 Evanescent wave modes with high reflection coefficients and their associated dispersion curves as – undamaged section, - - - damaged section. Red vertical lines indicate the frequencies of high reflection peaks.

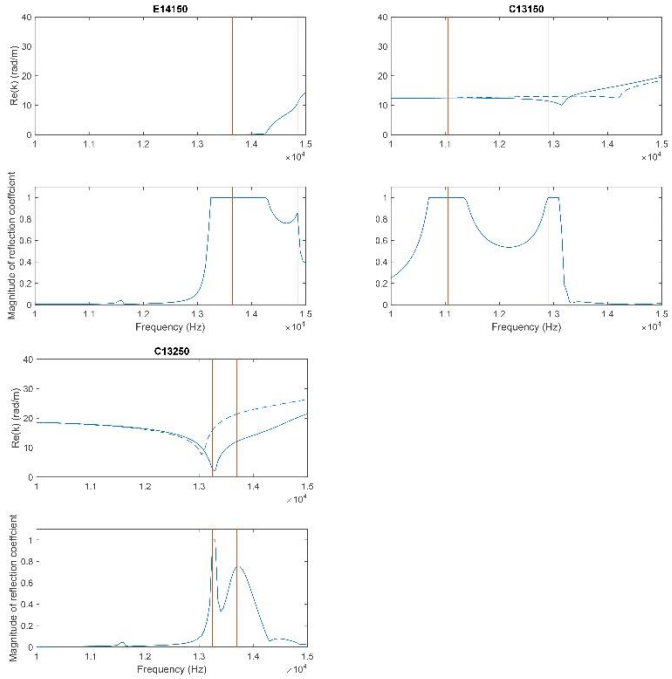

Figure 13 Complex wave modes with high reflection coefficients and their associated dispersion curves as – undamaged section, - - - damaged section. Red vertical lines indicate the frequencies of high reflection peaks.

First, partial debonding between CFRP and concrete causes a shift in the cut-on frequencies of evanescent and complex wave modes between the damaged and undamaged waveguides. For instance, this shift was to the right as seen in Figure 12 and Figure 13 for E11800, E13000, E14150 and C13150. This means that those waves start to propagate in the undamaged waveguide at a

prior frequency than the damaged ones. This results in high magnitude of reflection coefficients in the first peaks associated with those modes at the cut-on frequency shifts between the damaged and undamaged waveguides. On the other hand, C13250 had demonstrated a shift to the left in the cut-on frequency due to the introduction of partial bonding loss between CFRP and concrete. This means that the associated wave starts to propagate in the damaged waveguide at frequency prior to the undamaged one. This results in a first peak due to this frequency shift.

Second, the damage introduced results in difference in the wavenumbers between the damaged and undamaged waveguides. This is clear in E10350 and E13000. In both cases, the wavenumbers of the undamaged section are higher than the damaged ones for each step frequency after the cut-on. This means that the waves group velocity of is higher in the damaged waveguide than the undamaged ones. This difference have led to a high reflection coefficients in the last peaks of these wave modes as illustrated in Figure 12.

Third, the remaining of the peaks of wave modes with high reflection coefficients occur at frequencies where the wave mode propagating in the undamaged section interferes with another mode in the damaged section. Both wave modes possess the same wavenumber at this particular frequency. For example, in Figure 14, both waves modes E14150 in the undamaged waveguide and C15100 in the damaged one share the same wavenumber value at the frequency of 14150 Hz at which the wave mode E14150 had shown a high magnitude of reflection coefficient. Travelling at the same group velocity at 14850 Hz, E14150 had established major nodal displacement in the X direction. However, C15100 had shown minimal nodal displacement in the X-axis. This interference between the two modes and the difference in the wave modes displacement lead to high reflection of E14150. The same scenario occurs for the remaining peaks associated with E9100, E11800, E13150 and C13250.

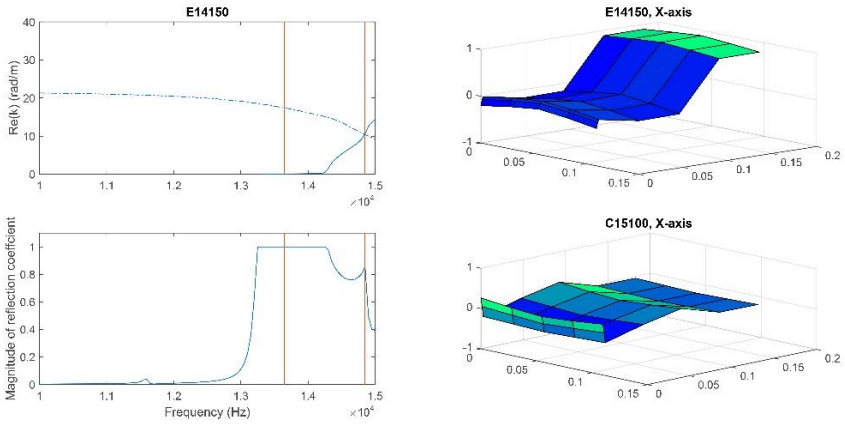

Figure 14 Dispersion curve of E14150 – undamaged section and C15100 - - - damaged section with their associated nodal displacements in the major direction. Magnitude of reflection coefficients of E14150. Vertical lines indicate the frequencies of peaks of reflection coefficients.

Subsequently, higher order modes as evanescent and complex wave modes have shown sensitivity to partial debonding between the CFRP and concrete over a specific length. This was highlighted by their reflection coefficients due to the debonding near the mode cut-on frequencies. Those wave modes had shown a dominant displacement in one of the X, Y and Z directions at their cut-on frequencies.

5. Conclusions

The WFE method was applied to the CFRP-strengthened RC beam sections with and without damage in order to extract the associated wave characteristics. The damage was introduced as partial debonding between CFRP and concrete through reduction in the value of the ultimate shear stress associated with the interface element. For least attenuated waves, dispersion curves and mode shapes are plotted. It has been seen that partial debonding of the interface between CFRP and concrete causes changes in some of evanescent and complex wave modes wavenumbers especially at cut-on frequency. These wave mode shapes have revealed distinguished nodal displacement around the interface CRFP-concrete compared to the whole cross section deformed shape. Then, scattering matrix was formulated via the WFE-FE-WFE coupling approach and the reflection coefficients associated with the partial debonding were calculated at each step frequency. Higher order modes as evanescent and complex modes had demonstrated sensitivity to partial debonding through high magnitude of reflection coefficients. This was related to the shift in the cut-on frequencies, difference in the wavenumbers values and wave mode interference at the same frequency between damaged and undamaged waveguides. Future work should focus on picking up those wave modes at particular frequencies in experimental validation.

Author Contributions

The first author had conducted all the FE models, data and results processing and writing the paper content. The second author had reviewed the whole written content.

Competing Interests

The authors have declared that no competing interests exist.

References

1. Murali G, Pannirselvam N. Flexural strengthening of reinforced concrete beams using fibre reinforced polymer laminate: A review. ARPN J Eng Appl Sci. 2011; 6: 41-47.
2. Moein RS, Tasnimi AA. An analytical model for FRP debonding in strengthened RC beams under monotonic and cyclic loads. Int J Concrete Struct Mater. 2016; 10: 499-511.
3. Siddika A, Al Mamun MA, Alyousef R, Amran YM. Strengthening of reinforced concrete beams by using fiber-reinforced polymer composites: A review. J Build Eng. 2019; 25: 100798.
4. Zhou J, Bi F, Wang Z, Zhang J. Experimental investigation of size effect on mechanical properties of carbon fiber reinforced polymer (CFRP) confined concrete circular specimens. Constr Build Mater. 2016; 127: 643-652.
5. Teng X, Zhang YX. Nonlinear finite element analyses of FRP-strengthened concrete slabs under fixed-point cyclic loading. J Compos Constr. 2015; 19: 04014057.
6. Ascione F, Lamberti M, Napoli A, Razaqpur G, Realfonzo R. An experimental investigation on the bond behavior of steel reinforced polymers on concrete substrate. Compos Struct. 2017; 181: 58-72.

7. Ascione F, Lamberti M, Napoli A, Razaqpur AG, Realfonzo R. Modeling SRP-concrete interfacial bond behavior and strength. Eng Struct. 2019; 187: 220-230.
8. Razaqpur AG, Lamberti M, Ascione F. Debonding evolution in nonlinear FRP-retrofitted RC beams with cohesive interface. Eng Struct. 2020; 236: 111858.
9. Razaqpur AG, Lamberti M, Ascione F. A nonlinear semi-analytical model for predicting debonding of FRP laminates from RC beams subjected to uniform or concentrated load. Constr Build Mater. 2020; 233: 117838.
10. Kharkovsky S, Ryley AC, Stephen V, Zoughi R. Dual-polarized near-field microwave reflectometer for noninvasive inspection of carbon fiber reinforced polymer-strengthened structures. IEEE Trans Instrum Meas. 2007; 57: 168-175.
11. Halabe UB, Vasudevan A, Klinkhachorn P, GangaRao HV. Detection of subsurface defects in fiber reinforced polymer composite bridge decks using digital infrared thermography. Nondestruct Test Eval. 2007; 22: 155-175.
12. Lai WL, Lee KK, Kou SC, Poon CS, Tsang WF. A study of full-field debond behaviour and durability of CFRP-concrete composite beams by pulsed infrared thermography (IRT). NDT E Int. 2012; 52: 112-121.
13. Yu TY, Büyüköztürk O. A far-field airborne radar NDT technique for detecting debonding in GFRP-retrofitted concrete structures. NDT E Int. 2008; 41: 10-24.
14. Degala S, Rizzo P, Ramanathan K, Harries KA. Acoustic emission monitoring of CFRP reinforced concrete slabs. Constr Build Mater. 2009; 23: 2016-2026.
15. Qiu Q, Lau D. The sensitivity of acoustic-laser technique for detecting the defects in CFRP-bonded concrete systems. J Nondestruct Eval. 2016; 35: 33.
16. Hsieh CT, Lin Y, Lin SK. Impact-echo method for the deterioration evaluation of near-surface mounted CFRP strengthening under outdoor exposure conditions. Mater Struct. 2017; 50: 72.
17. Jiang T, Kong Q, Patil D, Luo Z, L, Song G. Detection of debonding between fiber reinforced polymer bar and concrete structure using piezoceramic transducers and wavelet packet analysis. IEEE Sens J. 2017; 17: 1992-1998.
18. Wang Y, Zhu X, Hao H, Ou J. Guided wave propagation and spectral element method for debonding damage assessment in RC structures. J Sound Vibr. 2009; 324: 751-772.
19. Wang Y, Hao H. Modelling of guided wave propagation with spectral element: Application in structural engineering. AMM. 2014; 553: 687-692.
20. Wang Y, Li X, Li J, Wang Q, Xu B, Deng J. Debonding damage detection of the CFRP-concrete interface based on piezoelectric ceramics by the wave-based method. Constr Build Mater. 2019; 210: 514-524.
21. Giri P, Kharkovsky S, Zhu X, Clark SM, Samali B. Debonding detection in a carbon fibre reinforced concrete structure using guided waves. Smart Mater Struct. 2019; 28: 045020.
22. Renno JM, Mace BR. On the forced response of waveguides using the wave and finite element method. J Sound Vibr. 2010; 329: 5474-5488.
23. Duhamel D, Mace BR, Brennan MJ. Finite element analysis of the vibrations of waveguides and periodic structures. J Sound Vibr. 2006; 294: 205-220.
24. Waki Y, Mace BR, Brennan MJ. Numerical issues concerning the wave and finite element method for free and forced vibrations of waveguides. J Sound Vibr. 2009; 327: 92-108.
25. ANSYS Mechanical APDL, 201315, ANSYS Mechanical APDL element reference. Anleitung, Canonsburg USA: ANSYS Inc.

26. El Masri E, Ferguson N, Waters T. Wave propagation and scattering in reinforced concrete beams. J Acoust Soc Am. 2019; 146: 3283-3294.
27. Shrestha R. Behaviour of RC beam-column connections retrofitted with FRP strips. Sydney: University of Technology Sydney; 2009.
28. Lin X, Zhang YS, Pathak P. Nonlinear finite element analysis of composite and reinforced concrete beams. 1st ed. Cambridge: Woodhead Publishing; 2019.
29. Hawileh RA, Naser MZ, Abdalla JA. Finite element simulation of reinforced concrete beams externally strengthened with short-length CFRP plates. Compos Part B Eng. 2013; 45: 1722-1730.
30. Bedon C. Issues on the vibration analysis of in-service laminated glass structures: Analytical, experimental and numerical investigations on delaminated beams. Appl Sci. 2019; 9: 3928.
31. Xu XP, Needleman A. Numerical simulations of fast crack growth in brittle solids. J Mech Phys Solids. 1994; 42: 1397-1434.
32. Nakaba K, Kanakubo T, Furuta T, Yoshizawa H. Bond behavior between fiber-reinforced polymer laminates and concrete. Struct J. 2001; 98: 359-367.
33. El Masri E. Wave propagation in reinforced concrete beams with application to non-destructive testing. Southampton: University of Southampton; 2018.
34. Waki Y. On the application of finite element analysis to wave motion in one-dimensional waveguides. Southampton: University of Southampton; 2007.
35. Renno JM, Mace BR. Calculation of reflection and transmission coefficients of joints using a hybrid finite element/wave and finite element approach. J Sound Vibr. 2013; 332: 2149-2164.